PCCP

ROYAL SOCIETY OF CHEMISTRY

PAPER

View Article Online
View Journal | View Issue

Cite this: *Phys. Chem. Chem. Phys.*, 2021, **23**, 1401

Theoretical insights into non-oxidative propane dehydrogenation over Fe_3C†

Peng Wang and Thomas P. Senftle *

Identifying catalysts for non-oxidative propane dehydrogenation has become increasingly important due to the increasing demand for propylene coupled to decreasing propylene production from steam cracking as we shift to lighter hydrocarbon feedstocks. Commercialized propane dehydrogenation (PDH) catalysts are based on Pt or Cr, which are expensive or toxic, respectively. Recent experimental work has demonstrated that earth-abundant and environmentally-benign metals, such as iron, form *in situ* carbide phases that exhibit good activity and high selectivity for PDH. In this work, we used density functional theory (DFT) to better understand why the PDH reaction is highly selective on Fe_3C surfaces. We use *ab initio* thermodynamics to identify stable Fe_3C surface terminations as a function of reaction conditions, which then serve as our models for investigating rate-determining and selectivity-determining kinetic barriers during PDH. We find that carbon-rich surfaces show much higher selectivity for propylene production over competing cracking reactions compared to iron-rich surfaces, which is determined by comparing the propylene desorption barrier to the C–H scission barrier for dehydrogenation steps beyond propylene. Electronic structure analyses of the d-band center and the crystal orbital Hamilton population (COHP) of the carbides demonstrate that the high selectivity of carbon-rich surfaces originates from the disruption of surface Fe ensembles *via* carbon. Finally, we investigated the role of phosphate in suppressing coke formation and found that the electron-withdrawing character of phosphate destabilizes surface carbon.

Received 4th September 2020,
Accepted 17th December 2020

DOI: 10.1039/d0cp04669h

rsc.li/pccp

1 Introduction

Propylene is an important industrial precursor because it serves as the basis for numerous commodity-producing processes, including polymerization, addition, and oxidation reactions.[1,2] The demand for propylene has increased steadily,[1] yet supply has fallen during the shale gas revolution because propylene is a less prevalent by-product from the cracking of light hydrocarbons compared to naphtha.[3] Catalytic propane dehydrogenation (PDH) has drawn great attention as an alternative route for meeting market demand.[1,3,4] The most well-studied and commercialized catalysts for PDH are based on Pt[4] and Cr,[5] which are expensive and environmentally hazardous, respectively.[6–8] Thus, there is a pressing need to identify earth-abundant and environmentally-benign alternative catalysts for PDH.

Researchers recently have identified promising PDH catalysts with comparable selectivity and activity to commercialized catalysts based on inexpensive and non-toxic iron-based materials, including Fe or Fe_2O_3 supported by sulfated alumina,[7,8] iron-silica zeolites,[9] single-site Fe atoms on silica,[10] and iron nanoparticles derived from metal–organic frameworks on carbon supports.[11] Of particular interest to our present study, Tan *et al.*[6] found that phosphate-stabilized Fe_3C can achieve PDH selectivity to propylene as high as 80% and 20% conversion of propane. Using pre- and post-reaction X-ray diffraction (XRD), they reported that Fe_3C phases form *in situ* after an induction period on stream, which they postulated was responsible for the high observed selectivity. However, the underlying cause at the atomistic level for the high selectivity of Fe_3C, and the role of phosphate, remains unknown. The detailed surface structure of the catalyst during the induction period remains unclear. Here, we report a computational investigation of the PDH reaction mechanism on Fe_3C surfaces to better understand how this material achieves high PDH selectivity. We employ density functional theory (DFT) to investigate the thermodynamic stability of various iron carbide surface phases and their kinetic activity under PDH reaction conditions. Multiple computational studies have focused on stoichiometric terminations of various Fe_3C facets.[12–14] In this work we consider both stoichiometric and non-stoichiometric terminations that can persist under the carbon-rich conditions of the PDH reaction. We draw inspiration from the Fischer–Tropsch literature, where many studies have applied *ab initio* thermodynamics to

Department of Chemical and Biomolecular Engineering, Rice University, Houston, TX, 77005, USA. E-mail: tsenftle@rice.edu

† Electronic supplementary information (ESI) available. See DOI: 10.1039/d0cp04669h

determine the nature of stable surfaces under carbon-rich conditions, which affects the adsorption behavior of hydrocarbons on these surfaces.[14–17]

We first compare the surface energy of numerous possible terminations of $Fe_3C(001)$, $Fe_3C(010)$, $Fe_3C(011)$ facets as a function of carbon chemical potential. Having determined the most stable terminations and relative stability of the surfaces, we then compute and compare reaction energy paths for PDH on the most relevant terminations under reaction conditions. We find that the carbon-rich surfaces are more stable under the carbon-rich reaction environment, and that these surfaces generally show high selectivity for propylene due to a combined decrease in the propylene binding energy and an increase in deep dehydrogenation barriers. We analyze the electronic structure and bonding characteristics on these surfaces using the crystal orbital Hamilton population (COHP) and the d-band center of surface iron atoms, which reveals that a geometric effect dominates the propylene binding strength. Surface carbon disrupts large ensembles of surface Fe atoms, which limits the ability of propylene to form strong di-σ bonds that facilitate C–H bond scission. Compared to benchmark computations on Pt(111), these results predict that carbon-rich Fe_3C terminations are highly selective for PDH, indicating that Fe_3C is a potential alternative catalyst for PDH. The suppression of surface carbon by phosphate and analysis of charge transfer shows that phosphate weakens the Fe–C interaction to destabilize surface carbon atom and prevent coking.

2 Methods

2.1 Computational settings

All DFT calculations were completed in the Vienna *ab initio* simulation package (VASP 5.4.4).[18] The exchange–correlation energy was described by the Perdew–Burke–Ernzerhof (PBE)[19] generalized gradient approximation and projector-augmented-wave (PAW) theory[20] was employed with VASP default potentials[21] to treat frozen-core electrons. Valence electrons of Fe ($4s^1 3d^7$), C ($2s^2 2p^2$), H ($1s^1$), and Pt ($6s^1 5d^9$) were treated self-consistently throughout this work with a plane-wave basis set truncated at 450 eV. The kinetic energy cutoff was increased by 30% when optimizing bulk lattice parameters to mitigate artifacts arising from Pulay stress. Brilluoin zones were treated with Monkhorst–Pack *k*-point meshes,[22] which are summarized in Table S1 of the ESI.† All calculations were spin-polarized and the initial magnetic moment was set to be 20% greater than experimental values for Fe and Fe_3C phases.[23,24] Fe and Fe_3C are both metallic in nature,[25] where the metallic nature of Fe_3C is evident in Fig. S4 (ESI†). First order Methfessel–Paxton smearing[26] with a 0.2 eV width was applied to accelerate self-consist-field cycle convergence. The DFT-D3 method of Grimme[27] was employed in all calculations to treat van der Waals interactions, unless otherwise noted. Slabs are separated by a vacuum of at least 20 Å and a dipole correction was applied perpendicular to the slab in all surface model calculations. Optimized geometries were found by minimizing forces to <0.02 eV $Å^{-1}$. All adsorbed species were confirmed to be true energy minima with a frequency analysis using finite differences with a step size of 0.015 Å to ensure that no imaginary vibrational modes were present. Only components of the Hessian matrix for atoms in the adsorbed molecule were calculated and contributions from surface atoms were neglected. Transition state structures were found with the climbing image nudged elastic band (cNEB) method[28,29] and refined with the dimer method.[30] Saddle points were confirmed with a frequency analysis to ensure that there was one imaginary frequency along the reaction coordinate. The COHP method was implemented with the Lobster[31–34] code to analyze the binding characteristics of C_3H_6 on the different surfaces and C* atom binding on the Fe(110) surface. All energies, geometries, and imaginary frequencies of saddle points are reported in the ESI.†

2.2 Surface model construction

The bulk structures used in this paper are summarized in Table 1. The optimized lattice parameters in this table were used to construct all surface slab models. Surface energies were computed with mirrored slabs, where atoms on both sides of the slab were permitted to relax so that both sides of the slab represent the relaxed surface geometry. Slab thickness was determined by ensuring that the surface energy was converged to within 0.01 eV $Å^{-2}$. The adsorption energy of C_3H_x (x = 8, 7, 6, 5, 4) molecules and kinetic barriers were investigated on Fe(110), $Fe_3C(010)$, $Fe_3C(001)$, and $Fe_3C(011)$ surfaces identified from an *ab initio* thermodynamics analysis of stability (discussed below). These calculations employed a (2 × 2) supercell for Fe(110), $Fe_3C(010)$, and Pt(111), and a (2 × 1) supercell for $Fe_3C(001)$ and $Fe_3C(011)$. Adsorption energy calculations employed thinner slabs compared to the surface energy calculations for computational efficiency, where the bottommost layers of the slab were fixed in their bulk position. The number of frozen atoms and the *k*-point mesh of each surface model are summarized in Table S1 (ESI†). Artifacts from the reduced slab thickness and frozen layers largely cancel when computing adsorption

Table 1 Bulk structures of iron, iron carbide, and platinum

Composition	Space group	Lattice constant[a] (Å)			Lattice angle (°)			Magnetics
		a	*b*	*c*	*α*	*β*	*γ*	
Fe	$Im\bar{3}m$		2.806 [2.866][35]		90°			FM[b]
Fe_3C	*Pnma*	5.008 [5.077]	6.637 [6.765]	4.446 [4.518][36]	90°			FM
Pt	$Fm\bar{3}m$		3.917 [3.923][37]		90°			—

[a] The values in square brackets are the experimental references. [b] Ferromagnetic (FM).

energies, with adsorption energies that are within ~0.01 eV of those computed on the full mirrored slabs.

2.3 *Ab initio* thermodynamics

Periodic surface models of $Fe_3C(010)$, $Fe_3C(001)$, and $Fe_3C(011)$ with Fe-rich or C-rich terminations were built to evaluate the surface stability of iron carbide in the PDH environment through the formalism of *ab initio* thermodynamics. The details of this formalism are described in detail by Sholl and Steckel[38] and by Reuter.[39] In principle, the catalyst surface is in dynamic equilibrium with the reaction environment so that the chemical potential of any species on the catalyst surface must be equal to the chemical potential of that species in the gas phase. We define the surface free energy with respect to the chemical potential of all constituent species:

$$\gamma_{\text{surface}} = \frac{1}{2A}(E_{\text{slab}} - n_{\text{Fe}} \cdot \mu_{\text{Fe}} - n_{\text{C}} \cdot \mu_{\text{C}}) \quad (1)$$

and then use the equilibrium constraint to relate the chemical potential of carbon to the chemical potential of propane and hydrogen in the gas phase:

$$\mu_{\text{C}} = \frac{1}{3}(\mu_{C_3H_8} - 4\mu_{H_2}) \quad (2)$$

$$\mu_{\text{Fe}} = \frac{1}{3}(\mu_{Fe_3C} - \mu_{\text{C}}) \quad (3)$$

γ_{surface} is the surface free energy, A is the surface area of the termination in the calculation cell multiplied by two to account for both sides of the slab, E_{slab} is the total DFT energy of the symmetric slab with identical terminations on both sides, which is used to approximate the free energy of the slab, n_{Fe} is the number of Fe atoms in the slab, μ_{Fe} is the chemical potential of Fe, n_{C} is the number of C atoms in the slab, μ_{C} is the chemical potential of C, $\mu_{C_3H_8}$ is the chemical potential of gaseous propane, μ_{H_2} is the chemical potential of gaseous hydrogen, and μ_{Fe_3C} is the chemical potential of bulk iron carbide per formula unit. The chemical potential of bulk iron carbide is approximated by the total DFT energy of Fe_3C (*i.e.*, $\mu_{Fe_3C} = E^{\text{DFT}}_{Fe_3C}$) and the chemical potential of propane and hydrogen in the gas phase are computed with the following relationships:

$$\mu_{H_2} = E^{\text{DFT}}_{H_2} + \text{ZPVE} + \Delta H_{0\text{K}\rightarrow 873.15\text{K}} - TS_{873.15\text{K}} + RT \cdot \ln\frac{P_{H_2}}{P_{\text{ref}}} \quad (4)$$

$$\mu_{C_3H_8} = E^{\text{DFT}}_{C_3H_8} + \text{ZPVE} + \Delta H_{0\text{K}\rightarrow 873.15\text{K}} - TS_{873.15\text{K}} + RT \cdot \ln\frac{P_{C_3H_8}}{P_{\text{ref}}} \quad (5)$$

$E^{\text{DFT}}_{H_2}$ is the DFT energy of the H_2 molecule, ZPVE is the zero-point vibrational energy, $\Delta H_{0\text{K}\rightarrow 873.15\text{K}}$ is the enthalpy change of the molecule from 0 K to 873.15 K, T is the temperature, $S_{873.15\text{K}}$ is the entropy of the gas at 873.15 K, R is the gas constant, P_{H_2} is the partial pressure of H_2, P_{ref} is the reference pressure (1 atm), $E^{\text{DFT}}_{C_3H_8}$ is the total DFT energy of the C_3H_8 molecule, and $P_{C_3H_8}$ is the partial pressure of C_3H_8.

Similarly, to determine the stable coverage of surface carbon, the relative free energy is defined as:

$$\Delta G = E_{\text{adsorption}} - E_{\text{clean}} - n_{\text{C}}\mu_{\text{C}} \quad (6)$$

where ΔG is the relative free energy, $E_{\text{adsorption}}$ is the DFT energy of the surface with carbon adsorption, and E_{clean} is the DFT energy of the surface without carbon.

3 Results and discussion

3.1 Fe_3C termination stability

Combining eqn (1) and (3) above, we see that the computed surface free energy of stoichiometric terminations will be independent of the chemical potential of carbon because we use stoichiometric Fe_3C bulk as the reference. The surface free energy of surfaces with Fe : C ratios less than 3 : 1 will become more stable with increasing carbon chemical potential, as they become more stable under carbon-rich conditions. Only surfaces of Fe_3C that can be formed without reconstruction with respect to the bulk lattice positions (*i.e.*, surfaces that are formed by cleaving the bulk without further rearrangement other than local relaxation) are considered in this work. We chose to investigate the $Fe_3C(001)$ and $Fe_3C(010)$ facets because they are predicted to be stable in previous theoretical studies,[12–14] and we chose the $Fe_3C(011)$ facet because it was prominent in the XRD patterns collected *ex situ* after PDH in the experimental work of Tan *et al.*[6] Four, three, and eight distinct terminations were identified for the Miller planes of $Fe_3C(001)$, $Fe_3C(010)$, and $Fe_3C(011)$, respectively, as shown in Fig. 1. To name the facets defined in the figure, we use CR, IR, and ST to indicate carbon-rich, iron-rich, and stoichiometric surfaces, respectively, and when multiple CR or ST terminations are possible we use numbers to differentiate the surfaces (*e.g.*, "(011)-CR-3" represents the third carbon-rich surface of the (011) facet).

The comparison of the surface free energies with respect to the partial pressure of propane is shown in Fig. 2. On all three considered facets, carbon-rich terminations are favored thermodynamically under reaction conditions, where the $Fe_3C(010)$-CR surface is found to be the most stable among all the terminations. The higher stability of carbon-rich surfaces is the result of both saturating undercoordinated Fe atoms and the highly carbon-rich reaction environments. These results suggest that extra carbon on the surfaces is thermodynamically stable under PDH conditions, which agrees with experimental observations showing that coke or carbon nanotubes form readily on iron and iron carbide in carbon-rich environments.[6,10,40] The results also imply that coke will form readily on Fe and Fe_3C, which must be suppressed to maintain activity and selectivity. For instance, severe coking on the catalyst was observed on pure Fe during control experiments reported by Tan *et al.*, while the addition of phosphate suppressed the coking formation.[6]

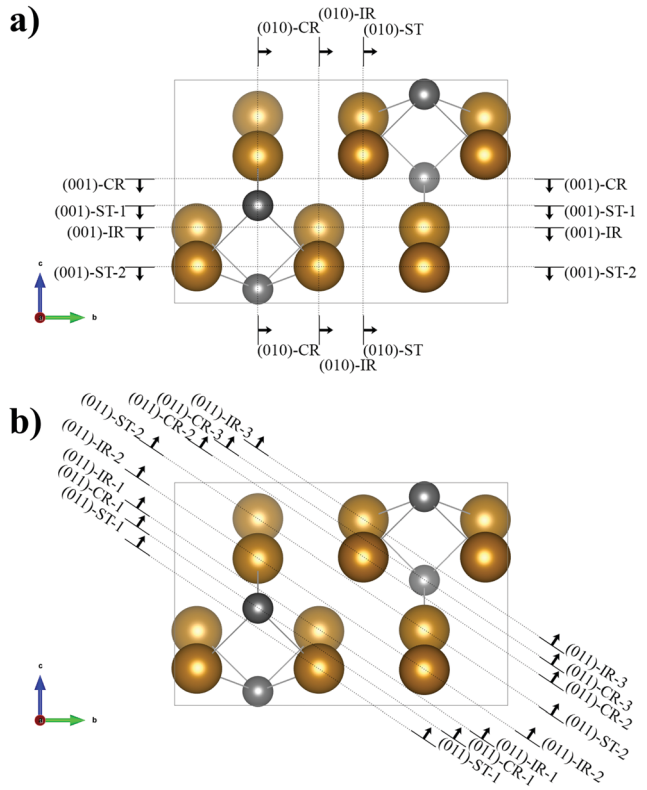

Fig. 1 Scheme for generating different terminations of the (a) $Fe_3C(001)$, $Fe_3C(010)$, and (b) $Fe_3C(011)$ facets. Dotted lines and arrows indicate the cleavage point and surface direction, where atoms centered on the line are the topmost atoms of the termination. Brown atoms are Fe and gray atoms are C; variation in the color intensity represents the atom depth.

The $Fe_3C(010)$-CR surface has the lowest surface free energy among all evaluated terminations, in agreement with computations reported by Ramo *et al.*[13] The five most stable surface terminations under reaction conditions that are relevant for investigating PDH kinetics include three carbon-rich surfaces ($Fe_3C(010)$-CR, $Fe_3C(001)$-CR, and $Fe_3C(011)$-CR-3) and two stoichiometric surfaces ($Fe_3C(001)$-ST-1 and $Fe_3C(011)$-ST-1). We also studied PDH kinetics over the Fe(110) surface for comparison. The top and side views of the five selected surfaces are shown in Fig. 3–5, which show that there is a significant difference in the size and shape of Fe surface ensembles between the different terminations (*e.g.*, as highlighted in the figure with red boxes). The ensembles are limited to a linear configuration on all carbon-rich surfaces because of the high carbon coverage, and are limited to a similar corrugated alignment on $Fe_3C(011)$-ST-1. In contrast, a large surface Fe ensemble area can be identified on $Fe_3C(001)$-ST-1 that resembles the Fe(110) surface. We find that these Fe ensembles at the topmost layer serve as the primary hydrocarbon adsorption site. As shown in the adsorption configurations in Fig. S5–S10 (ESI†), the adsorption of C_3H_x (x = 8, 7, 6, 5, 4) requires more connections to surface Fe atoms as the value of x decreases. Thus, larger ensembles of Fe can provide more bonding sites that will stabilize intermediates that have been dehydrogenated beyond propylene.

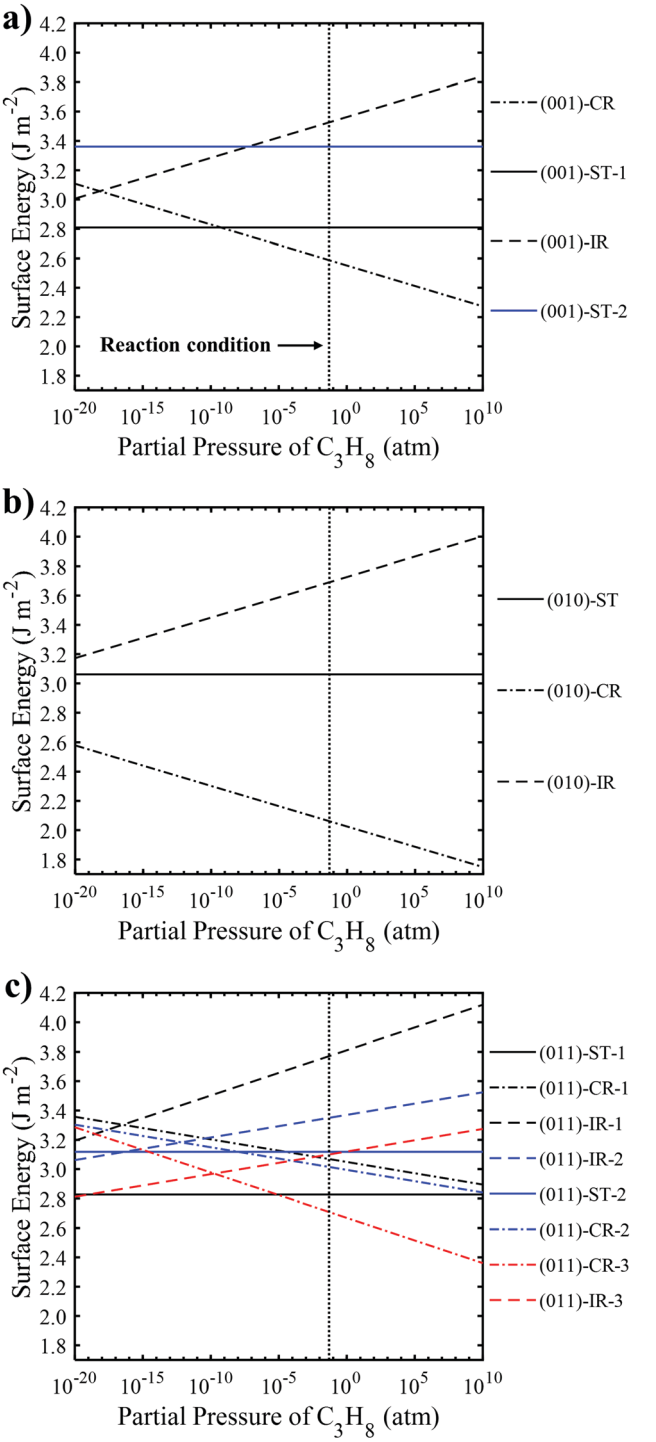

Fig. 2 The surface free energy of (a) $Fe_3C(001)$ (b) $Fe_3C(010)$, and (c) $Fe_3C(011)$ relative to the partial pressure of propane at 873.15 K and 0.01 atm H_2. Solid lines represent stoichiometric (ST) surfaces, dashed lines represent iron-rich (IR) surfaces, and dash-dotted lines represent carbon-rich (CR) surfaces. The reaction condition where the propane pressure is 0.05 atm is shown with the vertical black dotted line.

3.2 PDH reaction barriers

A schematic of the propane dehydrogenation mechanism is shown in Fig. 6. Achieving selective PDH requires sites on

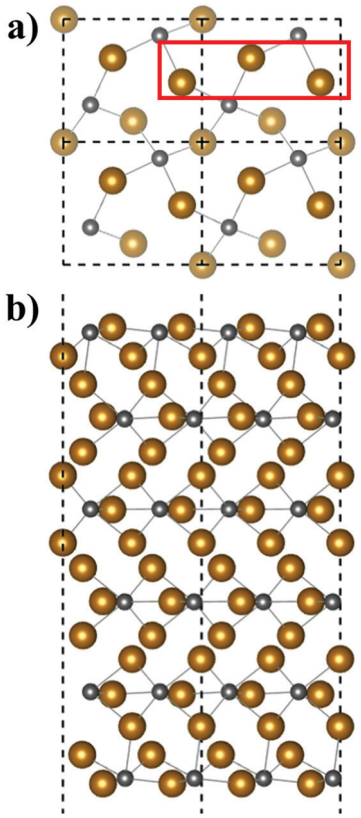

Fig. 3 (a) Top and (b) side view of the $Fe_3C(010)$-CR slab model. The intensity of atoms in the top view represents the position of the atom in depth. The unit cell is shown with a dashed line. The largest ensemble of iron atoms on the surface is marked in red on the top view.

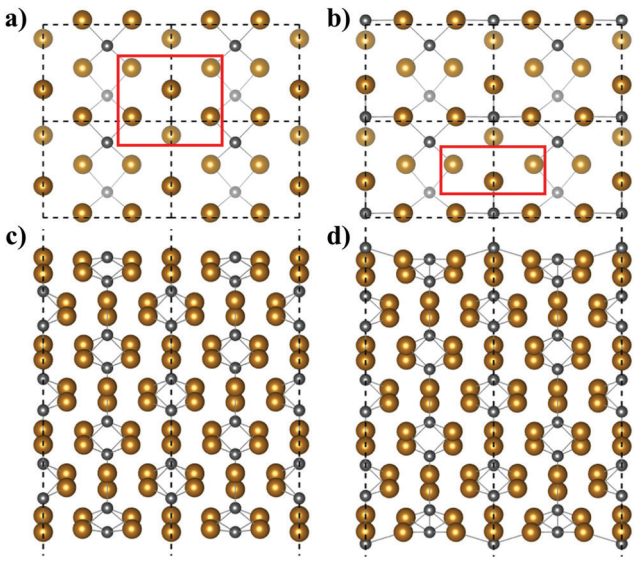

Fig. 4 (a) Top and (c) side view of $Fe_3C(001)$-ST-1, and (b) top and (d) side view of $Fe_3C(001)$-CR.

which the desorption of propylene is favored over further propylene dehydrogenation. As such, selectivity can be estimated by computing the difference between the barriers either

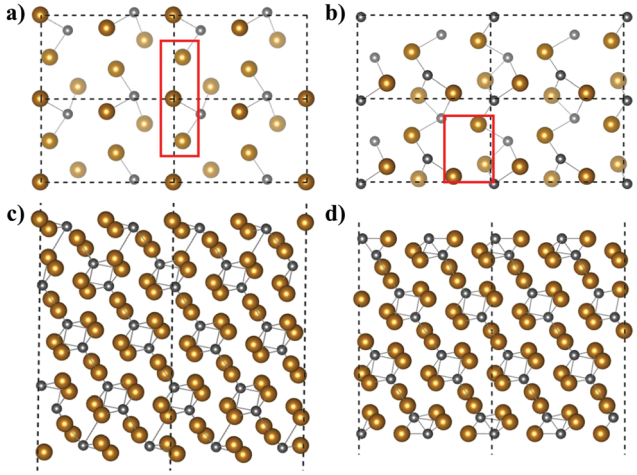

Fig. 5 (a) Top and (c) side view of $Fe_3C(011)$-ST-1, and (b) top and (d) side view of $Fe_3C(011)$-CR-3.

to desorb or to dehydrogenate propylene (*i.e.*, $C_3H_6^* \rightarrow C_3H_{6\,(g)} + *$ *versus* $C_3H_6^* + * \rightarrow C_3H_5^* + H^*$). Examples of this approach in the literature can be found in Sun *et al.*[41] and Yang *et al.*[42] The activity of the catalyst can be determined by the first propane dehydrogenation barrier, which includes both C_3H_8 physisorption and C–H bond scission steps. Zha *et al.*[43] reported an inverse relationship between these two metrics of activity and selectivity over Pt-based catalysts, as expected. Here, we will evaluate this relationship over the Fe and Fe_3C surface and compare to Pt(111) as a reference.

We investigated the PDH reaction pathway on six surfaces: five stable Fe_3C terminations and the clean Fe(110) surface. The reaction path was built using the most stable adsorption configurations of each intermediate, which was determined by considering all feasible adsorption geometries and adsorption sites. Details of the possible adsorption geometries of all intermediates on the various surfaces are further discussed in the ESI† and are summarized in Table S2. The dehydrogenation reaction network for propane is complex, as multiple C–H bonds can be broken. Here, we consider a simplified reaction network including elementary dehydrogenation steps between reaction intermediates of C_3H_x (x = 8, 7, 6, 5, 4). Both CH_3–CH_2–CH_2 (1-propyl) and CH_3–CH–CH_3 (2-propyl) were considered for the adsorption of C_3H_7 and the most stable adsorption configuration is taken to represent the reaction intermediate. The comparison of the formation energy of 1-propyl and 2-propyl is reported in Table S5 (ESI†) and a comparison of C–C bond-breaking steps *versus* C–H bond-breaking steps is reported in Fig. S1 (ESI†), where C–H bond-breaking steps are always more favorable (ESI†). Similarly, both CH_3–C–CH_2 (2-propenyl) and CH_3–CH–CH (1-propenyl) were considered for the adsorption of C_3H_5. Only CH_3–CH–CH_2 (propylene) is considered for C_3H_6 and only CH_3–C–CH (propyne) is considered for C_3H_4. The reaction energy diagrams on each surface are shown in Fig. 7, which includes the adsorption energy of C_3H_x (x = 8, 7, 6, 5, 4) as well as the transition states for each elementary dehydrogenation step. The y-axis shows the relative free energy along

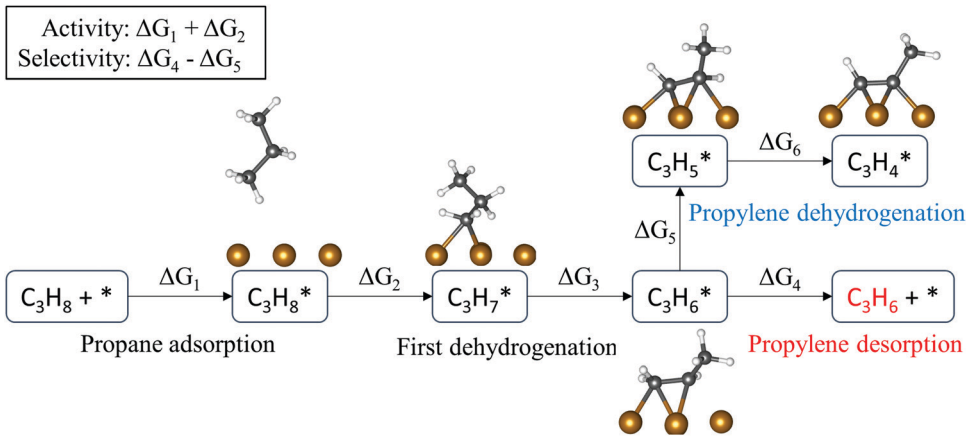

Fig. 6 Simplified reaction network of catalytic propane dehydrogenation. The selectivity of propylene is determined by the difference between the propylene dehydrogenation barrier and the propylene desorption barrier (*i.e.*, $\Delta G_4 - \Delta G_5$). The activity is determined by the apparent barrier for propane adsorption and dehydrogenation (*i.e.*, $\Delta G_1 + \Delta G_2$). The adsorption configurations on Fe(110) are shown here as representative examples.

the reaction coordinate referenced to gas phase propane and adsorbed hydrogen atoms, as defined by eqn (7):

$$\Delta G = G_{C3Hx^*} + (8 - x)\cdot G_{H^*} - (9 - x)E_* - G_{C3H8(g)} \quad (7)$$

The DFT energies of each adsorbed intermediate on the surface was computed in a separate cell, so all adsorbate-adsorbate interactions between hydrogen and the hydrocarbon are neglected in Fig. 7. Because of the large impact of entropy under high temperature, the propylene surface gas with 2-dimensional (2D) translational entropy is taken as the transition state for propylene desorption. On Fe_3C(010)-CR (Fig. 7d), Fe_3C(001)-CR (Fig. 7e), and Fe_3C(011)-CR-3 (Fig. 7f), the 2D surface gas is more stable than adsorbed C_3H_6 so the desorption step is considered to be barrierless for those steps.

The insets show the most stable configuration of each reaction step, which indicates that more bonds are formed between the hydrocarbon and the surface as dehydrogenation progresses. Detailed geometries are shown in Fig. S5–S10 (ESI†) and all energies used in the figures are reported in Table S4 (ESI†). The trends in the figure imply that deeper dehydrogenation is preferred on surfaces with larger iron ensembles that provide more binding sites for the molecule. This agrees with the exothermic reaction trend evident in the reaction energy diagrams on Fe(110) (Fig. 7a) and Fe_3C(001)-ST-1 (Fig. 7b), which both feature large Fe ensembles. As seen in the insets of these figures, the hydrocarbon adsorption geometries are also similar on these two surfaces. In contrast, hydrocarbon binding on the other four surfaces is clearly limited on the small, linear iron ensembles. Correspondingly, the propylene selectivity on the carbon-rich surfaces is much higher, as shown in Fig. 8a. The selectivity for propylene is determined by the difference between the propylene dehydrogenation barrier and the propylene desorption barrier, where more positive values indicate greater selectivity. In Fig. 8a, the surfaces are organized according to stability under reaction conditions (873.15 K, 0.05 atm C_3H_8, and 0.01 atm H_2). On the first three carbon-rich surfaces, which are most stable, the propylene dehydrogenation barriers (blue bars) are much higher than the desorption barriers (red bars), which suggests the dehydrogenation of propane on these surface will stop at this step because it is more favorable for propylene to desorb. On the other three surfaces, the dehydrogenation barrier is comparable to the desorption barrier. This is especially true on the two surfaces with large iron ensembles, Fe_3C(001)-ST-1 and Fe(110), indicating that these surfaces will not be selective toward propylene. In the previous section, the carbon-rich terminations were found to have lower surface free energy under the reaction conditions, which means they will share a larger portion of exposed surface area on the catalyst. The carbon-rich surfaces were also found to have higher selectivity to propylene, as shown by the critical barriers in Fig. 8a. The two conclusions above corroborate the high selectivity of Fe_3C, as the most stable surface terminations are also the most selective terminations. The stability of the surface itself is not causally related to the selectivity, but the carbon-rich surfaces tend to be more stable under carbon-rich conditions and they exhibit higher selectivity.

As is usually the case, surfaces with higher selectivity tend to have lower activity. The iron and iron carbide surfaces show a trade-off relationship between activity and selectivity for PDH, as shown with the red dashed line in Fig. 8b, which is similar to the relationship for Pt-based catalysts observed by Zha *et al.*[43] The first dehydrogenation barrier (*i.e.*, the apparent activation barrier for $C_3H_{8(g)} + * \rightarrow C_3H_7* + H*$) is taken as the index of activity. The difference between the desorption barrier (*i.e.*, the barrier for $C_3H_6* \rightarrow C_3H_{6(g)} + *$) and the propylene dehydrogenation barrier (*i.e.*, the barrier for $C_3H_6* + * \rightarrow C_3H_5* + H*$) is the index of selectivity. For comparison, the first dehydrogenation barrier (ΔG_2), propylene desorption barrier (ΔG_4), and the propylene dehydrogenation barrier (ΔG_5) computed on the Pt(111) surface are 0.17 eV, 0.71 eV, and 0.68 eV, respectively, where the corresponding geometries are shown in Fig. S11 (ESI). The activity and selectivity of Pt(111) is shown as the black data point in Fig. 8b. We found a significant difference in

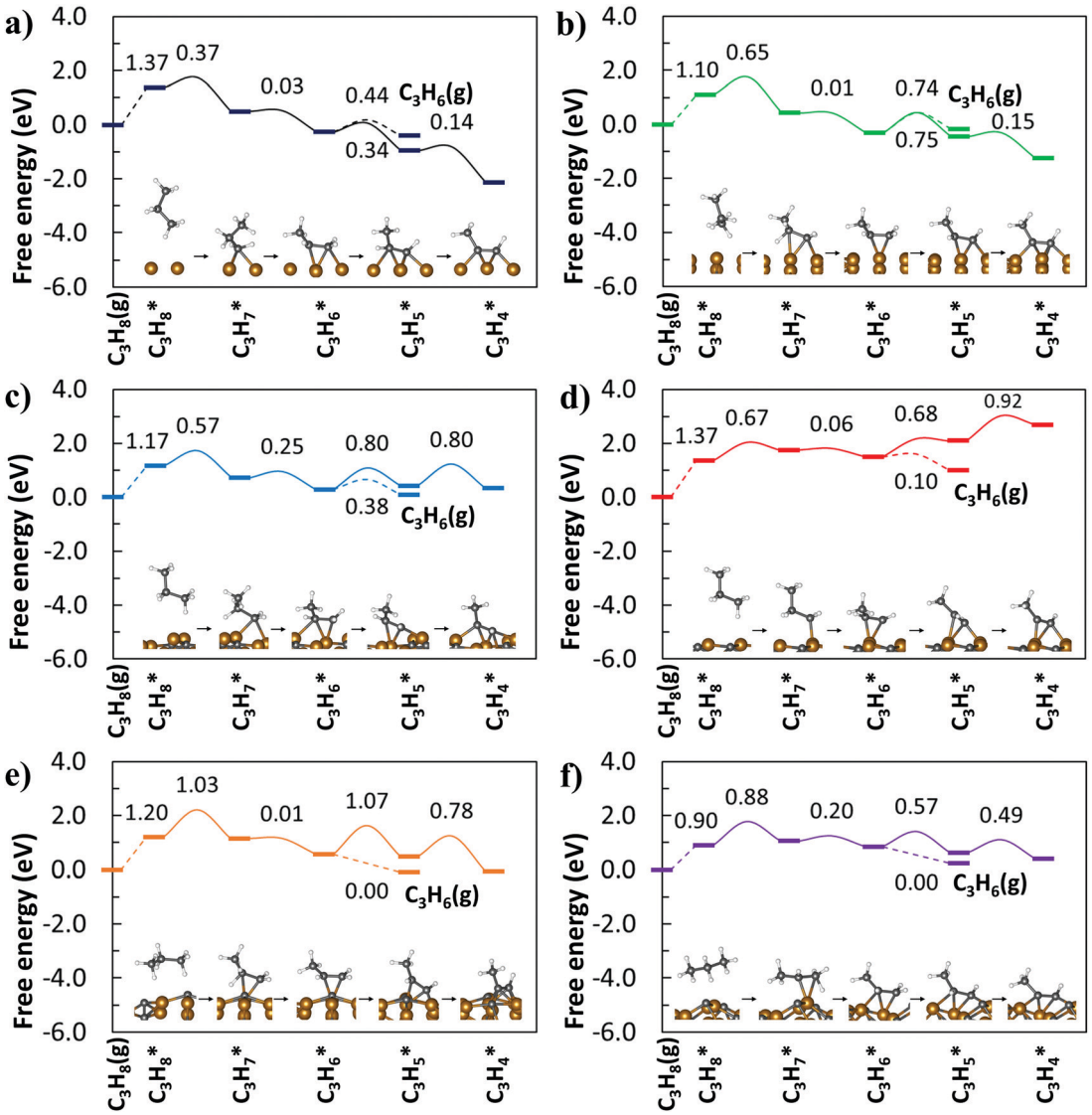

Fig. 7 Reaction energy diagram for PDH over (a) Fe(110), (b) Fe_3C(001)-ST-1, (c) Fe_3C(011)-ST-1, (d) Fe_3C(010)-CR, (e) Fe_3C(001)-CR, and (f) Fe_3C(011)-CR-3. The kinetic barriers are labeled for each step in eV. The adsorption and desorption processes are shown with dashed lines. The most stable configuration of each adsorption species is shown in the insets.

the propane physisorption energy on Pt(111) compared to the Fe and Fe_3C surfaces that was nearly entirely attributed to the D3 van der Waals energy correction, which causes Pt to have significantly lower apparent barrier for propane activation. Since there is some uncertainly in the empirical parameters of the D3 correction when it is applied to metal surfaces,[44] we also report this data with the van der Waals energy removed to determine if there are qualitative differences (Fig. 8c). We find that the activity–selectivity trend on Fe/Fe_3C is largely unaffected by the D3 correction, as the parameterization for Fe is consistent across these surfaces and thus only causes only a systematic shift in the data. We see that the Pt(111) data point falls closer to the Fe/Fe_3C trendline when the D3 correction is removed, but that the relative ordering of the data with respect to activity and selectivity is not changed. The Pt(111) surface falls close to the Fe/Fe_3C trendline in both cases, where Pt lies on the upper-left-hand corner of the trendline showing that it is more active and less selective compared to Fe_3C surfaces. In experimental studies on Pt surfaces, Ma *et al.*[45] observed 60% selectivity and 20% conversion and Zhu *et al.*[46] obtained 80% selectivity and 30% conversion. On Fe_3C surfaces, Tan *et al.*[6] found 80% selectivity and 20% conversion, which qualitatively agrees with the activity and selectivity trends predicted by our calculations. However, direct comparisons between these experimental results are tenuous, as they applied different experimental setups (*e.g.*, different supports, dopants, and temperatures). The general trends are in agreement with our computational results; namely, platinum is more active but less selective than Fe_3C surfaces.

3.3 Geometric effects on selectivity

The above results indicate that Fe_3C is selective toward propylene because (1) the high stability of carbon-rich terminations

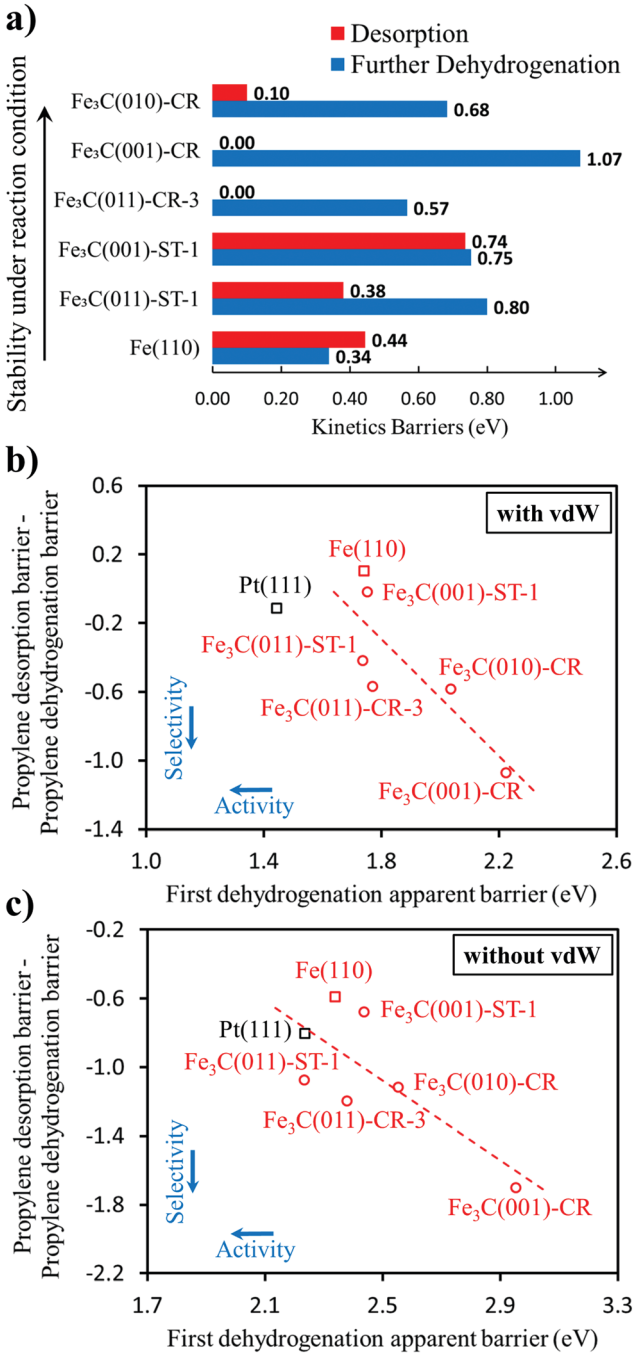

Fig. 8 (a) Comparison between the propylene desorption barrier and propylene dehydrogenation barrier on each surface. (b) Trade-off relationship between PDH selectivity and activity on Fe and Fe_3C surfaces (red) compared to Pt(111) (black). (c) Trade-off relationship between PDH selectivity and activity on Fe and Fe_3C surfaces (red) compared to Pt(111) (black) computed with van der Waals corrections removed.

under reactions conditions and (2) the reduced propylene binding energy on carbon-rich terminations. In this section we investigate more closely the binding behavior of propylene on these surfaces. Previous studies considering Pt-based PDH catalysts reported that activity and selectivity is promoted by the addition of inert metal atoms through either an electronic effect that stabilizes the d-state electrons of the active metal or a geometric effect that disrupts large ensembles of active metal atoms. For instance, the electronic effect of the inert atoms on the surface features a linear relationship between the adsorption energy of reaction intermediates (especially propylene) and the d-band centers of the catalyst surfaces.[42,43,47] The geometric effect was discussed in great detail in the application of a Pt/Sn alloy,[1,4,46,48–56] which is a popular commercialized catalyst for light alkane dehydrogenation. Numerous other examples are available in the literature, such as results reported by Cybulskis *et al.*[57] demonstrating that the addition of zinc in platinum can affect the reaction through both electronic and geometric effects, results from Yang *et al.*[58] showing that step sites promote deep dehydrogenation of propane on Pt, results from Gallagher *et al.*[59] attributing the increased selectivity of Pd/Zn to the geometrical isolation of Pd, or results from Ma *et al.*[45] showing the geometric effects of Cu on Pt, and Wegener *et al.*[60] showing the geometric effects In on Pt.

We propose that the high selectivity of carbon-rich surfaces is primarily the result of a geometric effect. Since the propylene dehydrogenation barriers on Fe_3C surfaces were found to have similar magnitudes, we focus on the propylene desorption barrier as the key descriptor for selectivity. We analyzed the bonding between C_3H_6 and Fe_3C surfaces using both a crystal orbital Hamilton population (COHP) method and the d-band centers of surface iron atoms. COHP allows one to analyze the molecule's binding strength to the surface by calculating the Hamilton-weighted density of states between any two atoms, where the integral of the COHP (ICOHP) represents the total amount of bonding/antibonding and is an index of bond strength.[61,62] The ICOHP between each pair of iron and carbon atoms within 3 Å were calculated to evaluate the bond strength, where more negative numbers indicate more bonding interactions than antibonding interactions and thus stronger binding. The d-band center of each surface Fe atom was computed on the clean surfaces without adsorbed propylene. Higher d-band center energies are expected to correlate with stronger adsorbate binding.[63]

The d-band center analysis of the Fe atoms on the clean surfaces are shown in Fig. 9. It is evident that surface Fe atoms on various Fe_3C surfaces have similar d-band centers (*i.e.*, ranging from −1.14 eV to −1.39 eV). This contrasts with the much higher d-band center on the Fe(110) surface (*i.e.*, −0.97 eV), which accounts for the higher activity and lower selectivity of Fe(110) compared to the Fe_3C surfaces. Yet, the effect of the d-band center is less important among the Fe_3C surfaces since they have similar d-band centers but exhibit significantly different propylene binding energies. For example, although they have similar Fe d-band centers, Fe_3C(001)-ST-1 shows a strong adsorption for propylene while the adsorption on Fe_3C(001)-CR is weak (*i.e.*, Fig. 9b *versus* Fig. 9e). Thus, the electronic effect is less important in the selectivity toward propylene on Fe_3C surfaces. This suggests that the strength of propylene adsorption on Fe_3C surfaces is determined by the surface geometry. A larger ensemble of iron on the surface allows the C_3H_6 molecule to form bonds with more iron atoms. For instance, a large Fe

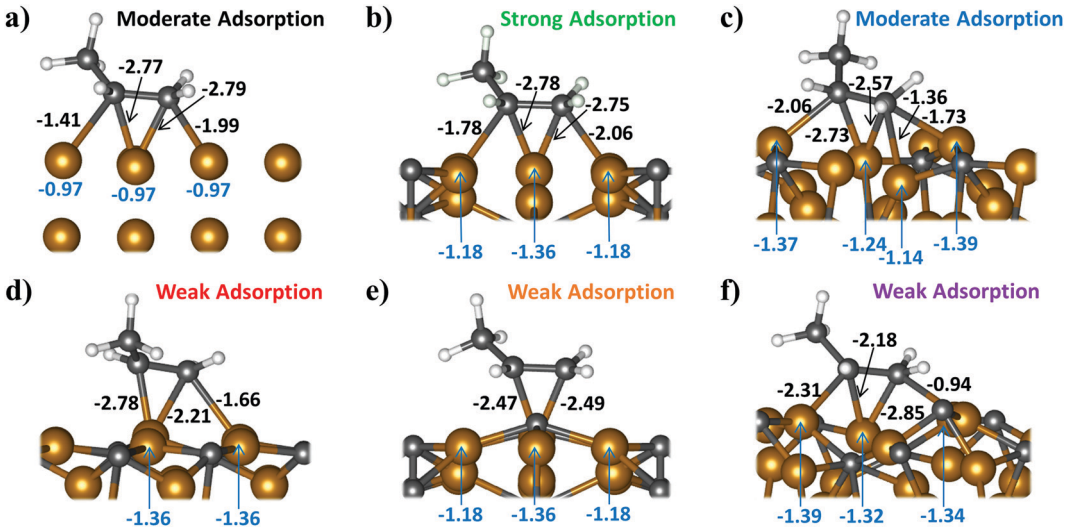

Fig. 9 The results of COHP and d-band center analysis on (a) Fe(110), (b) Fe_3C(001)-ST-1, (c) Fe_3C(011)-ST-1, (d) Fe_3C(010)-CR, (e) Fe_3C(001)-CR, and (f) Fe_3C(011)-CR-3. The values of ICOHP (black) of iron-carbon pairs within 3 Å are labeled next to the bonds in units of eV. The values of the d-band center (blue) of surface iron atoms are labeled in units of eV.

ensemble allows propylene to adsorb on the Fe_3C(001)-ST-1 surface in a di-σ mode (Fig. 9b), which is more stable than the π-binding mode on Fe_3C(001)-CR (Fig. 9e). Other than the separating effect of carbon atoms on carbon-rich surfaces, the geometric effect may also come from the alignment of surface atoms. For example, although both are stoichiometric surfaces, Fe_3C(011)-ST-1 (Fig. 9c) exhibits much weaker propylene adsorption compared to Fe_3C(001)-ST-1 (Fig. 9b) because some surface iron atoms on the latter surface are too deep within the surface structure to be accessible for propylene adsorption.

The change of density of states (DOS) for both the molecule and the surface during the adsorption were studied to further demonstrate how the geometric effect is acting on the stability of propylene adsorption, as shown in Fig. 10. The surfaces of Fe_3C(001)-ST-1 (Fig. 10a) and Fe_3C(001)-CR (Fig. 10b) are studied here for comparison because they have similar d-band centers of the surface Fe atoms, and the only difference between them is the extra surface carbon. There was a significant difference in the behavior of the molecular orbitals of propylene during the adsorption. On Fe_3C(001)-CR, the 2π orbital has a strong interaction with the surface and is entirely hybridized with the surface states, while all other orbitals remain in a similar position and do not interact with the surface. On Fe_3C(001)-ST-1, all orbitals from the 7σ to the 2π of propylene mix with the surface states. Thus, the geometric effect on carbon-rich surfaces limits the interaction between propylene and the surface to the hybridization of the 2π orbital forming the weak π-bonding mode. These results agree with known binding properties of propylene on Pt surfaces. For instance, Valcárcel *et al.*[64] found in their experiments that the binding of propylene on Pt(111) changed from a di-σ mode to a π-bonding mode with increased adsorbate coverage, which correlates with weaker adsorption strengths in the π-bonding mode compared to the di-σ mode. However, binding remains strong when the coverage is low enough to maintain the di-σ mode.

Either the electronic effect or the geometric effect can have more relative importance in different catalytic systems as discussed at the beginning of Section 3.3. In this work, we show that the geometric effect of surface carbon plays the most important role in determining the propylene selectivity on iron carbide surfaces, as it significantly influences the propylene adsorption strength. There is a weak electronic effect when comparing Fe to Fe_3C surfaces, as evident from the difference in the d-band center of surface Fe atoms. However, among Fe_3C surfaces the d-band center of surface Fe atoms is similar, and thus we find that the geometric effect is more important.

3.4 Effect of phosphate

In previous sections we have demonstrated that the ensemble effect reduced the propylene binding energy on the stable carbon-rich terminations. The unfavorable deep dehydrogenation on Fe_3C carbon-rich surfaces also implies that the Fe_3C phase has high resistance to coking, since the products of deep dehydrogenation, such as C_3H_5* or C_3H_4*, are the major sources of carbon for surface coking. During selective PDH over Fe_3C, all carbon introduced to the surface as propane leaves as propylene and there is no further carbon uptake. As shown in Fig. S2 (ESI†), on Fe(110) the calculated reaction energies for breaking C–H, C=C, and C–C bonds of C_3H_6* are −0.35 eV, −0.16 eV, and ∼0 eV, respectively, which indicates that the cracking reaction is very favorable on Fe(110). Thus, deep dehydrogenation and unselective cracking is preferred on pure iron surfaces, leading to rapid coke formation, as observed in experiment.[6,10] Tan *et al.* observe the formation of Fe_3C from pure Fe, where phosphate was added in the preparation of the catalysts.[6] During the initial reaction stage (0–30 min), the catalyst with phosphate shows high conversion of propane

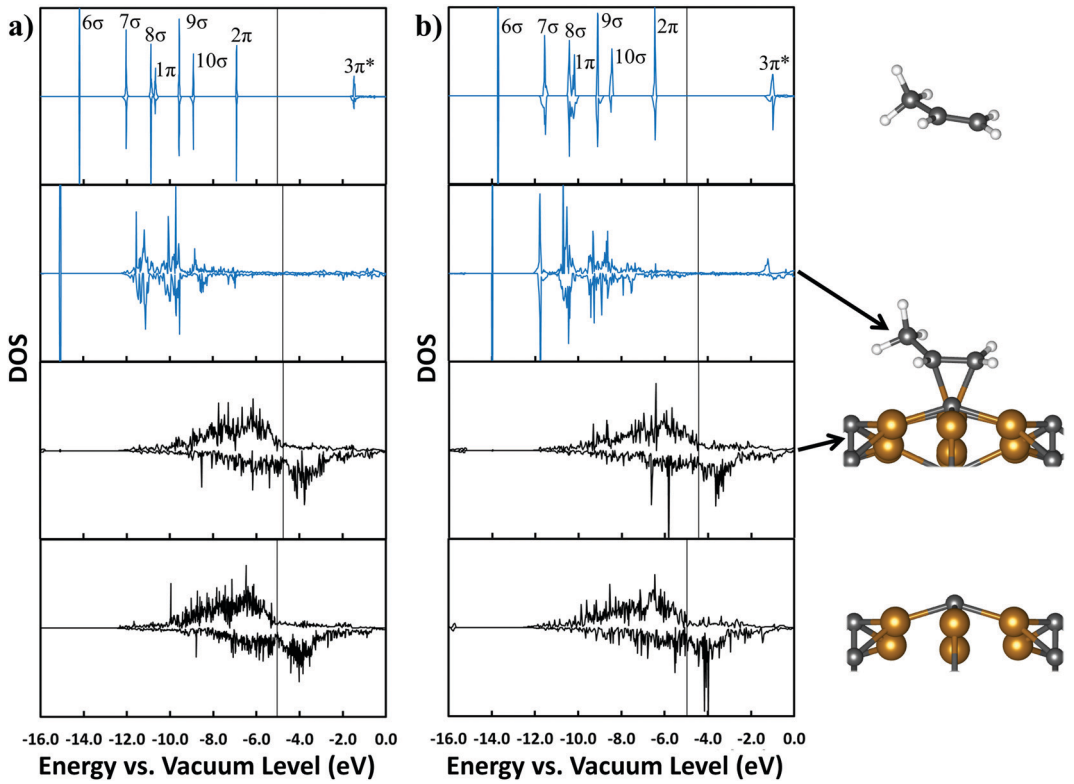

Fig. 10 DOS illustrating propylene bonding behavior on (a) $Fe_3C(001)$-ST-1 and (b) $Fe_3C(001)$-CR surfaces. The four panels in each case starting from the top are the DOS of a free molecule far away from the surface, of a molecule adsorbed on the surface, of the Fe atom d states on the surface with C_3H_6 adsorbed, and the Fe atom d states on a clean surface, respectively. The structures for $Fe_3C(001)$-CR are shown in the insets on the right side as examples. The *x*-axis is the energy *versus* the vacuum level. The *y*-axis is the DOS presented on different arbitrary scales in the different panels for legibility. The Fermi-level is indicated by the black vertical line.

and yields a large amount of hydrogen but no other gas products, which indicates that the catalyst has high activity for dehydrogenation and cracking similar to a pure iron surface. However, severe coking was not observed when phosphate was present, despite the carbon uptake by the catalyst. Furthermore, catalysts prepared with lower amounts of phosphate perform better than those with higher amounts of phosphate, suggesting that phosphate itself is not responsible for PDH activity. Thus, the phosphate's role is primarily to suppress coke formation as the Fe catalyst is transformed into the selective Fe_3C phase.

Here, we test the hypothesis that phosphate can prevent the accumulation of surface carbon on Fe facets. We used a Fe(110)-(2 × 2) model with a PO_4 group adsorbed on the surface to evaluate the phase diagram of the surface with varying C* coverage using *ab initio* thermodynamics, as shown in Fig. 11. The shaded area under the line of lowest energy indicates the stable carbon coverage with and without PO_4. The coverage of carbon is the C/Fe ratio on the topmost layer of Fe(110), where full monolayer (ML) coverage means all long-bridge sites on the surface are occupied with carbon. In Fig. 11a, the 1/4 ML coverage of carbon is stable down to 10^{-15} atm propane on the Fe surface with no phosphate. In Fig. 11b, the 1/8 ML coverage of carbon is stable to 10^{-7} atm propane and the 1/4 ML coverage is stable to 10^{14} atm propane on the surface with phosphate. Thus, the phosphate group on Fe(110) surface destabilizes surface carbon, shifting the region of high C* coverage outside the PDH reaction conditions. Phosphate can therefore prevent the accumulation of surface carbon and suppress coking. The effect of the protonation state of the phosphate (*i.e.*, HPO_4, H_2PO_4) on carbon adsorption was also tested, as shown in Fig. S3 (ESI†). The 1/4 ML coverage of carbon is stable to 10^{-6} atm propane with co-adsorbed H_2PO_4, and is stable to 10^{3} atm propane with co-adsorbed HPO_4. The protonated phosphate still destabilizes surface carbon but has less effect than the PO_4 group, which implies the destabilization of carbon is related to the amount of charge transfer.

PO_4 likely destabilizes surface C* *via* charge transfer, as the phosphate group is highly electron withdrawing in nature. To test this, the charge distribution of each configuration in Fig. 11 was analyzed using the Bader charge method,[65] as shown in Tables S3 and S4 (ESI†). Both the phosphate group and the surface carbon draw a large amount of electron density from the iron surface. For instance, when adsorbed on the Fe(110) surface, the carbon atom and phosphate group have −1.30 *e* and −2.00 *e* charge, respectively, where *e* is the positive elementary charge. Thus, there is competition for negative charge between the surface carbon and the phosphate. The charge of the PO_4 group changes to −1.97 *e* when a carbon atom is present, and the charge of the carbon atom changes to −1.21 *e* when phosphate is present. The strong charge transfer

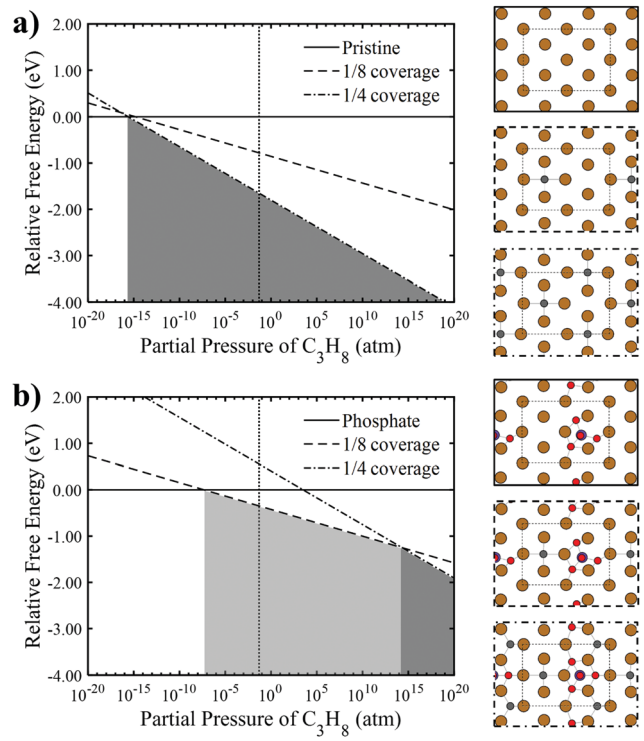

Fig. 11 Phase diagrams of surface carbon coverage on (a) pristine Fe(110) and (b) Fe(110) with PO_4 adsorbed. The solid line is the surface without carbon and is taken as the reference. The dashed line is the surface with one carbon atom per (2 × 2) cell. The dash-dotted line is the surface with two carbon atoms per (2 × 2) cell. The dotted vertical line is the reaction condition, which is at 873.15 K, 0.01 atm H_2, and 0.05 atm C_3H_8. The light gray area represents the stable region of 1/8 ML coverage of carbon and the dark gray area is for 1/4 ML coverage of carbon. The panels on the right side show the top view of the configurations corresponding to each line in the phase diagram. Brown: Fe, Red: O, Purple: P, Gray: C.

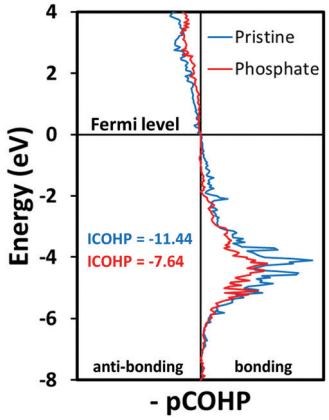

Fig. 12 pCOHP analysis of the bonding between C* and the four nearest surface Fe atoms with (red) or without (blue) phosphate co-adsorption.

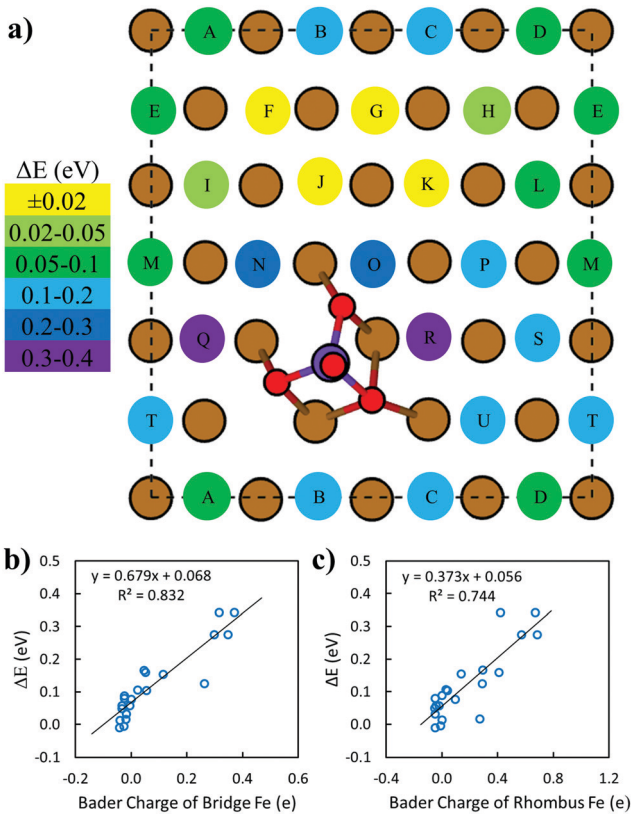

Fig. 13 (a) The change in carbon adsorption energy (ΔE) at each site caused by co-adsorption with phosphate. Darker color indicates a larger effect from the PO_4 group. (b) The correlation of ΔE with the total Bader charge of the two bridge Fe atoms of each site. (c) The correlation of ΔE with the total Bader charge of the four Fe atoms around the site.

toward phosphate destabilizes carbon on the surface by reducing the available charge density. We analyzed the bonding between the C* atom and the four nearest Fe atoms (1.8–2.1 Å) from the Fe(110) surface using the COHP method, as described in the previous section. The change to the Fe–C bond strength caused by the PO_4 group is shown in Fig. 12. On pristine Fe(110), C* can bond strongly since all occupied electronic states below the Fermi level are bonding in nature. When co-adsorbed with phosphate, the amount of bonding interactions between C* and the surface is decreased. As a result, the ICOHP value decreases from −11.44 eV to −7.64 eV. The effect of the van der Waals correction on COHP was tested for C* on Fe(110) and no difference was found. Combining the results from both Bader charge and COHP analyses, we conclude that the PO_4 group withdraws electron density and thus weakens the Fe–C carbon bond to destabilize surface carbon.

We used a larger surface model to study charge transfer as a function of distance from the PO_4 group (Fig. 13). On the Fe(110)-(4 × 3) surface, the effect of the phosphate is limited to its surrounding domain, as the charge of the surface Fe atoms varies with respect to position from the phosphate group. The carbon adsorption energy was calculated at each adsorption site shown in the figure, where Fig. 13a shows the change in the carbon adsorption energy (ΔE) at each site caused by co-adsorption with PO_4. The largest changes occur near the PO_4 group, suggesting that the charge transfer is mostly a local effect. We then correlated the change in adsorption energy with the Bader charge of the bridge Fe atoms at the site that form the shortest bond to the surface carbon (Fig. 13b)

or all four surrounding Fe atoms at the site (Fig. 13c). Both show high correlation with the change in carbon adsorption energy, which further shows that destabilization of surface carbon is the result of charge transfer.

4 Conclusion

In this work we demonstrate that the high selectivity of Fe_3C for propylene during PDH can be attributed to the high stability of carbon-rich surfaces under reaction conditions, as determined using *ab initio* thermodynamics. Kinetic barriers for the PDH reaction predict that these surfaces are highly selective toward propylene, where the difference in the desorption energy and dehydrogenation energy of propylene dictates selectivity. COHP and d-band center analyses together demonstrate that a geometric ensemble effect plays an important role because it determines the C_3H_6 adsorption strength. On Fe-based catalysts, carbon atoms from the environment form a stable carbide phase, which separates large iron ensembles that favor propylene adsorption and deep dehydrogenation. The demonstrated importance of the ensemble effect suggests that other iron-based compounds, such as iron sulfides/phosphides or iron alloys, are potential candidates for selective PDH. For instance, Wang *et al.*[66] examined seven different metal sulfides, including FeS, showing that several are selective catalysts for isobutene dehydrogenation with comparable performance to commercial catalysts. Other examples include the use of $Al_{13}Fe_4$ as an efficient catalyst for the hydrogenation of butadiene and acetylene.[67,68] Finally, we found that phosphate prevents rapid coking on pure iron surfaces *via* weakening the Fe–C interaction by withdrawing electron density from the surface.

Conflicts of interest

There are no conflicts to declare.

Acknowledgements

Acknowledgement is made to the Donors of the American Chemical Society Petroleum Research Fund (PRF #59759-DNI6) for support of this research.

References

1 J. J. H. B. Sattler, J. Ruiz-Martinez, E. Santillan-Jimenez and B. M. Weckhuysen, *Chem. Rev.*, 2014, **114**, 10613–10653.
2 B. M. Weckhuysen and R. A. Schoonheydt, *Catal. Today*, 1999, **51**, 223–232.
3 E. National Academies of Sciences, The Changing Landscape of Hydrocarbon Feedstocks for Chemical Production: Implications for Catalysis: Proceedings of a Workshop, 2016.
4 O. A. Barias, A. Holmen and E. A. Blekkan, *J. Catal.*, 1996, **158**, 1–12.
5 J. Gascón, C. Téllez, J. Herguido and M. Menéndez, *Appl. Catal., A*, 2003, **248**, 105–116.
6 S. Tan, B. Hu, W.-G. Kim, S. H. Pang, J. S. Moore, Y. Liu, R. S. Dixit, J. G. Pendergast, D. S. Sholl, S. Nair and C. W. Jones, *ACS Catal.*, 2016, **6**, 5673–5683.
7 Y. Sun, L. Tao, T. You, C. Li and H. Shan, *Chem. Eng. J.*, 2014, **244**, 145–151.
8 Y. Sun, Y. Wu, H. Shan, G. Wang and C. Li, *Catal. Sci. Technol.*, 2015, **5**, 1290–1298.
9 J. H. Yun and R. F. Lobo, *J. Catal.*, 2014, **312**, 263–270.
10 B. Hu, N. M. Schweitzer, G. Zhang, S. J. Kraft, D. J. Childers, M. P. Lanci, J. T. Miller and A. S. Hock, *ACS Catal.*, 2015, **5**, 3494–3503.
11 M. L. Sarazen and C. W. Jones, *J. Phys. Chem. C*, 2018, **122**, 28637–28644.
12 W. Chiou, *Surf. Sci.*, 2003, **530**, 88–100.
13 D. Muñoz Ramo and S. J. Jenkins, *J. Chem. Phys.*, 2017, **146**, 204703.
14 R. J. P. Broos, B. Klumpers, B. Zijlstra, I. A. W. Filot and E. J. M. Hensen, *Catal. Today*, 2019, S092058611831616X.
15 S. Zhao, X.-W. Liu, C.-F. Huo, Y.-W. Li, J. Wang and H. Jiao, *Catal. Struct. React.*, 2015, **1**, 44–59.
16 X.-Y. Liao, D.-B. Cao, S.-G. Wang, Z.-Y. Ma, Y.-W. Li, J. Wang and H. Jiao, *J. Mol. Catal. A: Chem.*, 2007, **269**, 169–178.
17 J. G. R. de la Cruz, M. K. Sabbe and M.-F. Reyniers, *J. Phys. Chem. C*, 2017, **121**, 25052–25063.
18 G. Kresse and J. Furthmüller, *Comput. Mater. Sci.*, 1996, **6**, 15–50.
19 J. P. Perdew, K. Burke and M. Ernzerhof, *Phys. Rev. Lett.*, 1996, **77**, 3865–3868.
20 P. E. Blöchl, *Phys. Rev. B: Condens. Matter Mater. Phys.*, 1994, **50**, 17953–17979.
21 G. Kresse and D. Joubert, *Phys. Rev. B: Condens. Matter Mater. Phys.*, 1999, **59**, 1758–1775.
22 H. J. Monkhorst and J. D. Pack, *Phys. Rev. B: Solid State*, 1976, **13**, 5188–5192.
23 R. Zeller, Spin-Polarized DFT Calculations and Magnetism, in *Computational Nanoscience: Do It Yourself!*, ed. J. Grotendorst, S. Blügel and D. Marx, John von Neumann Institute for Computing, 2006, pp. 419–445.
24 I. N. Shabanova and V. A. Trapeznikov, *J. Electron Spectrosc. Relat. Phenom.*, 1975, **6**, 297–307.
25 M.-C. Lee and G. Simkovich, *Metall. Trans. A*, 1987, **18**, 485–486.
26 M. Methfessel and A. T. Paxton, *Phys. Rev. B: Condens. Matter Mater. Phys.*, 1989, **40**, 3616–3621.
27 S. Grimme, J. Antony, S. Ehrlich and H. Krieg, *J. Chem. Phys.*, 2010, **132**, 154104.
28 G. Mills, H. Jónsson and G. K. Schenter, *Surf. Sci.*, 1995, **324**, 305–337.
29 H. Jónsson, G. Mills and K. W. Jacobsen, *Classical and Quantum Dynamics in Condensed Phase Simulations*, World Scientific, 1998, pp. 385–404.
30 G. Henkelman and H. Jónsson, *J. Chem. Phys.*, 1999, **111**, 7010–7022.
31 R. Dronskowski and P. E. Bloechl, *J. Phys. Chem.*, 1993, **97**, 8617–8624.

32 V. L. Deringer, A. L. Tchougréeff and R. Dronskowski, *J. Phys. Chem. A*, 2011, **115**, 5461–5466.
33 S. Maintz, V. L. Deringer, A. L. Tchougréeff and R. Dronskowski, *J. Comput. Chem.*, 2013, **34**, 2557–2567.
34 S. Maintz, V. L. Deringer, A. L. Tchougréeff and R. Dronskowski, *J. Comput. Chem.*, 2016, **37**, 1030–1035.
35 P. M. Giles, M. H. Longenbach and A. R. Marder, *J. Appl. Phys.*, 1971, **42**, 4290–4295.
36 I. G. Wood, L. Vočadlo, K. S. Knight, D. P. Dobson, W. G. Marshall, G. D. Price and J. Brodholt, *J. Appl. Crystallogr.*, 2004, **37**, 82–90.
37 K. H. Hong, G. M. McNally, M. Coduri and J. P. Attfield, *Z. Für Anorg. Allg. Chem.*, 2016, **642**, 1355–1358.
38 D. S. Sholl and J. A. Steckel, Equilibrium Phase Diagrams from Ab Initio Thermodynamics, in *Density Functional Theory*, ed. D.S. Sholl and J.A. Steckel, Wiley, 2009, pp 163–178.
39 K. Reuter, *Ab Initio* Thermodynamics and First-Principles Microkinetics for Surface Catalysis, in *Operando Research in Heterogeneous Catalysis*, ed. J. Frenken and I. Groot, Springer International Publishing, Cham, 2017, pp. 151–188.
40 R. J. Wrobel, A. Hełminiak, W. Arabczyk and U. Narkiewicz, *J. Phys. Chem. C*, 2014, **118**, 15434–15439.
41 G. Sun, Z.-J. Zhao, R. Mu, S. Zha, L. Li, S. Chen, K. Zang, J. Luo, Z. Li, S. C. Purdy, A. J. Kropf, J. T. Miller, L. Zeng and J. Gong, *Nat. Commun.*, 2018, **9**, 4454.
42 M.-L. Yang, Y.-A. Zhu, X.-G. Zhou, Z.-J. Sui and D. Chen, *ACS Catal.*, 2012, **2**, 1247–1258.
43 S. Zha, G. Sun, T. Wu, J. Zhao, Z.-J. Zhao and J. Gong, *Chem. Sci.*, 2018, **9**, 3925–3931.
44 R. L. H. Freire, D. Guedes-Sobrinho, A. Kiejna and J. L. F. Da Silva, *J. Phys. Chem. C*, 2018, **122**, 1577–1588.
45 Z. Ma, Z. Wu and J. T. Miller, *Catal. Struct. React.*, 2017, **3**, 43–53.
46 H. Zhu, D. H. Anjum, Q. Wang, E. Abou-Hamad, L. Emsley, H. Dong, P. Laveille, L. Li, A. K. Samal and J.-M. Basset, *J. Catal.*, 2014, **320**, 52–62.
47 L. Nykänen and K. Honkala, *J. Phys. Chem. C*, 2011, **115**, 9578–9586.
48 R. Burch and L. C. Garla, *J. Catal.*, 1981, **71**, 360–372.
49 F. H. Ribeiro, A. L. Bonivardi, C. Kim and G. A. Somorjai, *J. Catal.*, 1994, **150**, 186–198.
50 C. Xu and B. E. Koel, *Surf. Sci.*, 1994, **304**, 249–266.
51 A. L. Bonivardi, F. H. Ribeiro and G. A. Somorjai, *J. Catal.*, 1996, **160**, 269–278.
52 Y.-L. Tsai, C. Xu and B. E. Koel, *Surf. Sci.*, 1997, **385**, 37–59.
53 J. M. Hill, R. D. Cortright and J. A. Dumesic, *Appl. Catal., A*, 1998, **168**, 9–21.
54 F. Humblot, J. P. Candy, F. Le Peltier, B. Didillon and J. M. Basset, *J. Catal.*, 1998, **179**, 459–468.
55 R. D. Cortright, J. M. Hill and J. A. Dumesic, *Catal. Today*, 2000, **55**, 213–223.
56 A. Virnovskaia, S. Morandi, E. Rytter, G. Ghiotti and U. Olsbye, *J. Phys. Chem. C*, 2007, **111**, 14732–14742.
57 V. J. Cybulskis, B. C. Bukowski, H.-T. Tseng, J. R. Gallagher, Z. Wu, E. Wegener, A. J. Kropf, B. Ravel, F. H. Ribeiro, J. Greeley and J. T. Miller, *ACS Catal.*, 2017, **7**, 4173–4181.
58 M.-L. Yang, Y.-A. Zhu, C. Fan, Z.-J. Sui, D. Chen and X.-G. Zhou, *Phys. Chem. Chem. Phys.*, 2011, **13**, 3257–3267.
59 J. R. Gallagher, D. J. Childers, H. Zhao, R. E. Winans, R. J. Meyer and J. T. Miller, *Phys. Chem. Chem. Phys.*, 2015, **17**, 28144–28153.
60 E. C. Wegener, Z. Wu, H.-T. Tseng, J. R. Gallagher, Y. Ren, R. E. Diaz, F. H. Ribeiro and J. T. Miller, *Catal. Today*, 2018, **299**, 146–153.
61 A. Lücke, U. Gerstmann, T. D. Kühne and W. G. Schmidt, *J. Comput. Chem.*, 2017, **38**, 2276–2282.
62 R. Y. Rohling, I. C. Tranca, E. J. M. Hensen and E. A. Pidko, *J. Phys. Chem. C*, 2019, **123**, 2843–2854.
63 J. K. Nørskov, F. Abild-Pedersen, F. Studt and T. Bligaard, *Proc. Natl. Acad. Sci. U. S. A.*, 2011, **108**, 937–943.
64 A. Valcárcel, J. M. Ricart, A. Clotet, F. Illas, A. Markovits and C. Minot, *J. Catal.*, 2006, **241**, 115–122.
65 G. Henkelman, A. Arnaldsson and H. Jónsson, *Comput. Mater. Sci.*, 2006, **36**, 354–360.
66 G. Wang, C. Li and H. Shan, *ACS Catal.*, 2014, **4**, 1139–1143.
67 L. Piccolo, *Chem. Commun.*, 2013, **49**, 9149–9151.
68 M. Armbrüster, K. Kovnir, M. Friedrich, D. Teschner, G. Wowsnick, M. Hahne, P. Gille, L. Szentmiklósi, M. Feuerbacher, M. Heggen, F. Girgsdies, D. Rosenthal, R. Schlögl and Y. Grin, *Nat. Mater.*, 2012, **11**, 690–693.